HHS Public Access

Author manuscript

Ultrason Imaging. Author manuscript; available in PMC 2018 March 01.

Published in final edited form as:

Ultrason Imaging. 2017 March ; 39(2): 108–125. doi:10.1177/0161734616662227.

Virtual Breast Quasi-static Elastography (VBQE): A Case Study in Contrast Transfer Efficiency of Viscoelastic Imaging

David Rosen, **Yu Wang**, and **Jingfeng Jiang**

Department of Biomedical Engineering, Michigan Technological University

Abstract

Viscoelasticity Imaging (VEI) has been proposed to measure relaxation time constants for characterization of *in-vivo* breast lesions. In this technique, external compression forces on tissue being imaged are maintained for a fixed period of time to induce strain creep. A sequence of ultrasound echo signals are then utilized to generate time-resolved strain measurements. Relaxation time constants can be obtained by fitting local time-resolved strain measurements to a viscoelastic tissue model (*e.g.* a modified Kevin-Voigt model). In this study, our primary objective is to quantitatively evaluate the contrast transfer efficiency (CTE) of VEI, which contains useful information regarding image interpretations.

Using an open-source simulator for virtual breast quasi-static elastography (VBQE), we conducted a case study of contrast transfer efficiency of VEI. In multiple three-dimensional numerical breast phantoms containing various degrees of heterogeneity, finite element (FE) simulations in conjunction with quasi-linear viscoelastic constitutive tissue models were performed to mimic data acquisition of VEI under freehand scanning. Our results suggested that there were losses in CTE and the losses could be as high as -18 dB. FE results also qualitatively corroborated clinical observations, e.g. artifacts around tissue interfaces.

Keywords

Elastography; Finite Element Modeling; Viscoelastic Imaging; Breast Cancer

1. Introduction

In recent years, strain elastography (1-3) (SE) has been successfully applied to non-invasive differentiation of breast lesions (2, 4). In the framework of SE, speckle tracking (3, 5, 6) is first performed between echo signals acquired before and after tissue deformation. Then, local strains estimated from ultrasonically-measured displacements are used to infer the relative elastic stiffness of component tissues. To improve diagnostic accuracy (particularly specificity) of breast cancers, research efforts (7-10) have been expanded to include viscoelastic properties. Those research efforts are collectively named as viscoelastic imaging (VEI). VEI is accomplished by collecting a sequence of time-resolved strain images that are then used to estimate the strain creep (relaxation) time constant. Feasibility of VEI, as well

Corresponding Author: Jingfeng Jiang, Mineral and Material Sciences Building, RM.309, 1400, Townsend Drive, Houghton, Michigan 49931, United States of America jjiang1@mtu.edu Telephone: +1 90604871943.

as its basis in molecular cancer biology (7), has been demonstrated through phantom materials and *in vivo* breast tissues (7-10). Furthermore, in an early clinical trial (11), it was reported that VEI provided discrimination of malignancy in non-palpable breast tumors where SE did not.

Despite the above-mentioned progresses, some unknowns need to be addressed in order to further develop VEI toward its full potential. Toward this end, our primary objective of study is to understand the contrast transfer efficiency (CTE) of VEI. Using CTE simulations as a case study, we also want to demonstrate the usefulness of virtual breast quasi-static elastography VBQE (12). To our knowledge, the CTE of VEI has not be systemically investigated. CTE in elastography has been broadly defined as the ratio of (intensity) contrast produced in an image to the ideal or "true" contrast of the material property being measured (13). CTE has been a useful imaging parameter for characterizing the degree to which an elastographic technique captures the material property it intends to image, contributing to our understanding of contrast limits of SE (13, 14) and electrode-displacement elastography (15).

In this study, virtual imaging prototyping (*i.e.* VBQE) was used to investigate the CTE of VEI. Virtual imaging prototyping, a technique borrowed from manufacturing, is referred to a process of imaging system development, which involves computer-aided engineering software (*i.e.* geometry modeling and Finite Element Analysis [FEA] software) to validate a design or method before committing to making a physical/hardware prototype. This approach deviated from typical investigations into elastographic CTE in two ways. First, most prior studies used idealized tissue-mimicking (TM) or numerical phantoms composed of a simplistic geometrical target embedded in a large uniform background (13-15); VBQE is capable of efficiently simulating complex geometrical structures. Second, due to the difficulty in developing TM materials which represent realistic viscoelastic material properties, most prior studies used linearly elastic solids. VBQE has the capability to assign varying material properties. In short, it is important to consider the utility of more sophisticated tissue models which include anatomical structures and realistic material properties.

Because of practical difficulties and cost associated with developing complex TM phantoms that can realistically represent both the anatomy and material properties, VBQE becomes a viable alternate. However, only a few studies of this kind have been reported. This is largely due to the fact that building complex and anatomically-realistic VBQE models requires interdisciplinary knowledge in tissue mechanics, computer modeling, finite element modeling (FEM) and acoustic signal processing and is therefore difficult to conduct. One exception was presented by Bhatti and Sridhar-Keralapura (16). However, they used linearly elastic solids and idealized geometries (*e.g.* a half spherical virtual breast) to simulate the structure of the human, female breast. Now, an open-source VBQE simulation platform (12) can be used as a single gateway software platform to perform advanced VBQE simulations of this kind. In the VBQE platform, both realistic (*i.e.* heterogeneous) anatomy and sophisticated viscoelastic material models are available. Leveraging this resource, we expect to better understand the characteristics of CTE.

2. Materials and Methods

The proposed software workflow is a multiple step process (see Fig. 1). This process, along with interactions with numerical breast models and FEBio (17), are briefly presented in this section.

2.1 Finite Element (FE) Models

As shown in Fig. 1, the starting point is FE models. CTE was first investigated and characterized in simple FE phantom models, followed by CTE characterization in two complex breast phantoms modified from a previous publication (12). All geometries were defined by 3D triangulated surfaces generated by Visualization Toolkit (VTK, Kitware, Inc., NY) (19) and then meshed to tetrahedrons by an open-source mesh generator called Tetgen (verison 1.4.2; WIAS, Berlin, Germany) (20). More specifically, in the simple phantom model, a single spherical inclusion was embedded in a 60mm × 60mm × 60mm block, as depicted in Fig. 2. Geometries of two 3D complex virtual breast phantoms (*i.e.* Lesion 1 and Lesion 4 phantoms in our previous work(12)) were adopted for this study. The image plane of the Lesion 4 phantom is illustrated in Fig. 2. Both the Lesion 1 and Lesion 4 phantoms were developed based on landmarks (*e.g.* fibro-glandular region, skin *etc.*) from Magnetic Resonance Imaging (MRI) data (21), in addition to random small anatomical structures (*e.g.* Coopers' ligaments, milk ducts, *etc.*). Particularly, the Lesion 1 phantom represents a simulated breast tumor with regular margins, while the Lesion 4 phantom represents a simulated complex breast cancer with an irregular shape and a necrotic core. Details regarding the construction of both numerical breast phantoms can be found in a previous publication(12).

2.2 Finite Element (FE) Simulations

FE Simulations were conducted using an open-source non-linear FE solver (FEBio 2.0; University of Utah and Columbia University) (17) using a quasi-linear viscoelastic (QLV) material model (22). Simple and complex phantoms contains approximately 0.75 million and 2.5 million finite elements, respectively. A mesh sensitivity study was conducted in our previous study (12). Loosely speaking, this QLV constitutive model (22) includes both elastic and viscous components as shown in Table 1 below, with more details found in the Appendix. Particularly, we applied a constant force that was evenly distributed around the simulated contact surface (approximately 4 × 1.5 cm) between the ultrasound transducer and the corresponding phantom in all FE simulations. Typically, this compressional force was ramped from zero force to the specified target force over a 1 second period with or without pre-compressions. This force was then held constant for the duration of the simulation as the strain creep occurred. The force varied between 2 – 20 N to simulate different amounts of compressions (5% - 15%). This range is consistent with values reported in the literature (*e.g.* (8, 11))

To ensure that a given FE simulation ran long enough to precisely capture the overall shape of the relaxation time constant curve, an adaptive time scheme was devised. The total simulation would run for at least three times as long as the largest relaxation time among all material components after the initial 1 second force ramp. The adaptive time stepping

scheme also assured that the time step would be smaller than the smallest relaxation constant of all material components.

2.3 Estimation of Relaxation Time Constants

FE-simulated displacement data for each and every time step were exported from the FE solver (*i.e.* FEBio (17)) to reconstruct axial displacement fields in a uniform rectilinear grid (approximately 0.02 mm × 0.02 mm). One strain image from each time step was created from the axial displacement field associated with the time step using a two point finite difference scheme. Thus, one time-resolved strain curve (see the red curve in Fig. 3) for each and every spatial location/pixel was obtained. Each time-resolved strain curve was fitted into a modified Kevin-Voigt model (11) using the Optimization Toolbox in MATLAB (Mathworks Inc., MA, USA) as follows,

$$\varepsilon(t)=\varepsilon_0+\varepsilon_1\left[1-\exp\left(-t/T_1\right)\right] \quad (1)$$

where ε_0 is the instantaneous elastic strain that occurs immediately after compression and ε_1 is the amplitude of the exponential creep curve. In Eqn. (1), the constant T_1 is the relaxation time used in VEI (11). To clarify, the Kevin-Voigt model used in the (11) deviated from the conventional setting — one spring and one dashpot in parallel, because the instantaneous strain $\varepsilon(t)$ is not zero in Eqn. (1). In this study, we termed this model as a modified Kevin-Voigt model in order to keep our description consistent with the work by Qiu et al. (11) In fact, the creep strain curve under this modified Kevin-Voigt model (Eqn. (1)) is mathematically identical to a three-element (Kevin-form) standard linear Solid (SLS) model (24). The creep strain curve of the SLS model can be found in the Appendix.

2.4 Calculation of contrast transfer efficiency

Imaging contrast was calculated by averaging pixel values between selected regions-of-interests (ROIs) within the imaging target and in adjacent regions of the imaging background, with the total number of pixels averaged in the background being equal to that of the target. ROIs were placed in a similar position to (12, 18). The ROI within the imaging target was placed at the center of the imaging target, while the four ROI's placed in the imaging background were placed in an X pattern around the imaging target. The ROIs placed in the imaging background were offset from the target-background boundary in order to avoid boundary artifacts present in the image. A contrast value could then be calculated by dividing the average relaxation time constant collected from the target by that of the background.

CTE was defined similarly as it has been in other simulation studies of QUE (13, 25). The CTE is given by the following equation (15):

$$\mathrm{CTE}=|C_0(dB)|-|C_t(dB)| \quad (2)$$

Where C_o is the image contrast calculated in the VEI as described above, and C_t is the true image contrast between the background and the target due to a difference in the underlying material properties.

Results

FE Simulation results in this section are used to demonstrate characteristics of CTE and has been organized to address three aspects: (1) CTE characteristics in simple phantoms with linear stress-strain relations in the QLV constitutive model, (2) CTE characteristics in simple phantoms with nonlinear stress-strain relations in the QLV consistent model, and (3) CTE assessments in complex numerical breast phantoms.

3.1 Loss of CTE in Simple Phantoms with Linear Stress-strain Relations

In general, FE simulation results showed that there were losses in CTE while the relaxation time constant (RTC) of the target differed from that of its background. Fig. 4 displays an example of CTE results, taken from a set of Case 1 phantoms (see Table 1), where the elastic modulus ratio between the target and the background is approximately 5:1 for the Neo-Hookean model in the framework of QLV model (see Appendix). The RTC ratios between the target and the background were varied between -20 dB to 20 dB. In all cases, estimated contrast tended to diminish in points farther away from 0 dB of the true underlying contrast. Common to all cases, the characteristics of the lost contrast seemed to depend on the sign and absolute magnitude of the true contrast values. For positive contrasts, *i.e.* contrasts to the right of 0 dB, losses of CTE would approach a plateau and it would seem that a consistent bias in the imaged contrast would be observed. For negative contrast values, no such plateau was observed and CTE decreased with increasingly negative contrast values (Fig. 4).

Figure 5 displays basic characteristics of contrast transfer for three different (target-to-background) elastic modulus ratios: 1:1, 5:1 and 10:1. From these results, it is apparent that increased target stiffness relative to the background increased CTE throughout the range of contrasts simulated. It was clear that none of these scenarios produced ideal contrast transfer. Indeed, the CTE gains were more dramatic between 1:1 and 5:1 elastic moduli ratios than between 5:1 and 10:1.

Figure 6 displays simulation results for contrast transfer characteristics of Case 2 phantoms where the target size was varied. In all Case 2 phantom scenarios, the elastic modulus ratio between the target and the background was set at 5:1. From this we see that target diameter also contributed to the amount of contrast transferred into the RTC image, though not as dramatically as different elastic moduli ratios (see Fig. 5). More specifically, a larger inclusion diameter resulted in a greater amount of contrast transferred to the RTC image.

Since losses of contrast, as we have defined it, must be due to mischaracterization of the material relaxation time in either or both the imaging target and imaging background, it is worthwhile to consider values of the relaxation times which result in observed contrast transfer. This provides the necessary information to begin to decipher some of the underlying dynamics which result in lost CTE. Fig. 7 displays this information for both the varied target diameters and elastic moduli ratios. From this it is apparent that the majority

CTE loss is due to mischaracterization of the spherical imaging target rather than the background. In fact, RTC image pixels collected from the imaging background deviated inappreciably from their ideal values. One might also note a peculiar characteristic of the target relaxation which is that below roughly -12dB of true contrast the imaged relaxation time begins to increase rather than decrease. This observation was common to all Case 1 and Case 2 phantoms, the increase was much steeper for the scenarios with apparently improved contrast transfer characteristics (*i.e.* higher underlying elastic contrasts and larger target diameters.)

3.2 CTE characteristics in simple phantoms with nonlinear stress-strain relations

Fig. 8 illustrates effects that stress-strain nonlinearity and varied degrees of pre-compression (5%, 10% and 15%) had on contrast transfer characteristics in two Case 3 phantoms. One can see that, in the benign case where the target has similar degrees of nonlinearity to the background, there is not an appreciable difference in contrast transfer characteristics. Comparing this with the malignant case, where the imaging target is substantially more non-linear, we observe more appreciable CTE losses, with losses being greater for the larger compressions.

3.3 CTE assessments in complex numerical breast phantoms

Having established some basic characteristics of contrast transfer in the simple phantom model scenarios, characteristics of the complex phantom (*i.e.* Case 4 Phantoms) can now be interpreted with some context. Figures 9 and 10 display sample RTC images for the two different simulated lesions in the nearly identical background (*i.e.* simulated fibro-glandular tissues). From the Lesion 1 phantom one can see that the relaxation time contrast tends to be more homogenous throughout the simulated breast lesion. Indeed, if one considers Figure 11, it is apparent that the resulting CTE characteristics in the Lesion 1 phantom were within the range of CTE values observed in the Case 1 phantom. Of note, the initial elastic modulus ratio between the Lesion 1 and its fibro-glandular background was set to be 7.5:1 at the small strain, as shown in Table A1 in the Appendix.

For the Lesion 4 phantom, it is apparent that this relation is more complicated. The relaxation time appeared to vary more substantially throughout the lesion with artifacts appearing throughout, while the underlying relaxation time constant was assumed to be the same. For instance, the portion of the lesion which protrudes out of the glandular tissues and into the fatty tissue appears to have a lower contrast compared to the portions of the lesion imbedded more deeply into the fibro-glandular tissue. This observation is shown in Figure 12 (see Box 3 vs. Box 1).

3.4 Preliminary Results Regarding Changes in the Gamma Parameter

The influences of the parameter γ_1 (Eq. A2 in the Appendix) on CTE are investigated in this section. γ_1 determines the degree to which the material will relax after a mechanical stimulus is applied. Figure 13 displays CTE results as a function of γ_1, which was varied from 0.15 to 1.5 in the Case 1 phantom. The underlying VEI contrast was set to 20 dB and an elastic modulus ratio of 5:1 between the spherical target (diameter: 10 mm) and the background material. γ_1 was varied both throughout the material (Figure 13a) and within the

imaging target only (Figure 13b) with γ in the imaging background set to 0.95. While variations in this parameter did not display a major influence on the CTE when target and background matched, losses in CTE were prominent when γ_1 in the target was lower than the background material, appearing to level off with higher values of γ_1.

Discussion

This study, to our knowledge, is the first comprehensive FE simulation study into the CTE properties of VEI for characterization of breast tissue lesions. Results from our study improve understanding of VEI as a novel image modality, thereby aiding in its image interpretations. It was clear from these results that the contrast transfer characteristics observed were a result of the complex interactions between the imaging target and background. As shown in the Results section above (see Figs. 4-7), both the size of the imaging target and the underlying elastic contrast were significant factors in the contrast transferred in to the relaxation time constant (RTC) images. The dependence of VEI contrast on the purely elastic material properties of the target relative to background have some interesting consequences. Since malignant lesions such as invasive ductal carcinomas tend to be stiffer than benign lesions (26), it is likely that this effect may contribute to the specificity of VEI to characterizing dangerous lesions. Additionally, this suggests that it may be warranted to consider VEI in conjunction with modalities for characterizing purely elastic properties (*e.g.* SE and shear wave elastography[SWE]). A future study may consider how combining elastic and viscoelastic characterization as well as the CTE characteristics may be used to develop a better estimate of relaxation time as well as an estimate of characterization uncertainty. It is also interesting to note that the loss of contrast due to the target diameter would seem to indicate that VEI may be more accurate when it is used to image larger lesions than it is for small lesions. If this observation is true, VEI may not be able to characterize malignant lesions in early stages where the tumor is just beginning to grow.

Since malignant breast lesions typically have shorter relaxation times than their surrounding fibro-glandular tissues (7, 11), the larger loss of contrast for negative dB values of true contrast may hamper this effort. Additionally, one may have noticed that around -12dB true contrast, the imaged contrast actually begins to increase, meaning that the contrast observed in a relaxation time image may be associated with more than one relaxation time constant (see Fig. 7). In this sense, a quantitative use of lesion relaxation time constant for characterization of breast tumors could be challenging, similar to the situation when the strain ratio in SE was used as a means for breast lesions differentiation (4, 27).

The consequences of hyperelastic nonlinearity and degree of compression on CTE indicate that these factors may also contribute in important ways to the CTE of viscoelasticity. Of course, this issue may be mitigated when readings from force sensors can be used to provide feedbacks to the operator (11). From our simulation results, we can see that simple phantom characteristics are well suited for describing lesions which are relatively compact and regularly shaped near tissue boundaries. Significantly irregularly shaped lesions which protrude into different tissues can have significantly different CTE characteristics throughout the lesion, thereby complicating the image interpretation. Furthermore, imaging artifacts

around tissue interfaces were also clearly visible. Artifacts around tissue interfaces are likely due to complex interactions around the tissue interfaces where strain response curves deviate away from typical creep strain curves. Similar artifacts were also observed from previous *in vivo* studies (8, 11).

The current study was conducted to investigate the contrast transfer characteristics of VEI in a similar fashion to that which has been done in SE (13-15). We attributed those contrast losses to the fundamental continuum mechanics. However, our FE-based approach did not consider losses due to ultrasound image and subsequent speckle tracking. Those losses are typically small as compared to the contrast loss due to the continuum mechanics (13-15), though this can be considered a limitation of the current study.

Another possible limitation of the current study is the lack of a full investigation of the influence by the γ_1 parameter on CTE. The preliminary results presented here suggest that while γ_1 seems to display minor influences over CTE in the relaxation time image when it is identical for both the target and inclusion, it results in more dramatic losses when it is significantly smaller within the imaging target as compared to the inclusion. This would be expected, as a small γ_1 parameter implies the initial strain, and thus the initial stiffness of the model, would dominate over the viscous terms. Since γ_1 determines the amount of stain accumulated during material relaxation, it may be warranted to consider a full investigation γ_1 of with acoustic simulations. Detectability of small changes in time resolved strain in conjunction to acoustic simulations would shed light on detectability dependent on ultrasound systems. Nevertheless, relative viscoelastic changes over the time determined by γ_1 could be a factor in contrast losses due to the sensitivity and accuracy of ultrasonic speckle tracking.

Conclusions

In this study, we have used an FE-based approach to investigate the physics behind the contrast transfer efficiency of VEI. In general, we found that there were significant losses in CTE for nearly all cases investigated. More specifically, in some cases, the CTE losses could be as high as -18 dB. Our FE results also qualitatively corroborated clinical observations, *e.g.* artifacts around tissue interfaces. Overall, our FE-simulated results expands current understanding of the imaging characteristics intrinsic to the VEI technique, thereby aiding image interpretation.

Acknowledgments

This study is partially funded by US National Institute of Health (R15- CA179409).

Appendix Detailed Material Parameters Used for VEI Simulations

For FE-simulations of VEI, a quasi-linear viscoelastic (QLV) material model (24) was used for all FE simulation presented in this study. In the QLV model, the instantaneous stress $\sigma(t)$ at time t can be expressed as follows (28),

$$\sigma(t)=\int_{-\infty}^{t} G(t-\tau)\frac{\partial \sigma^{e}}{\partial \tau}d\tau \quad \text{(A1)}$$

$$G(t)=1+\sum_{i=1}^{N}\gamma_i \exp(-t/\tau_i) \quad \text{(A2)}$$

where σ^e is the elastic stress and $G(t)$ is a reduced stress relaxation function (22). In Eqn. (A2), τ_i represents one of relaxation time values in the Prony series, and γ_i is the viscoelastic coefficient in the Prony series. In this study, N was set to be 1 and Eqn. (A2) became a three-element Standard Linear Solid (SLS) model (24), as shown in Figure A1.

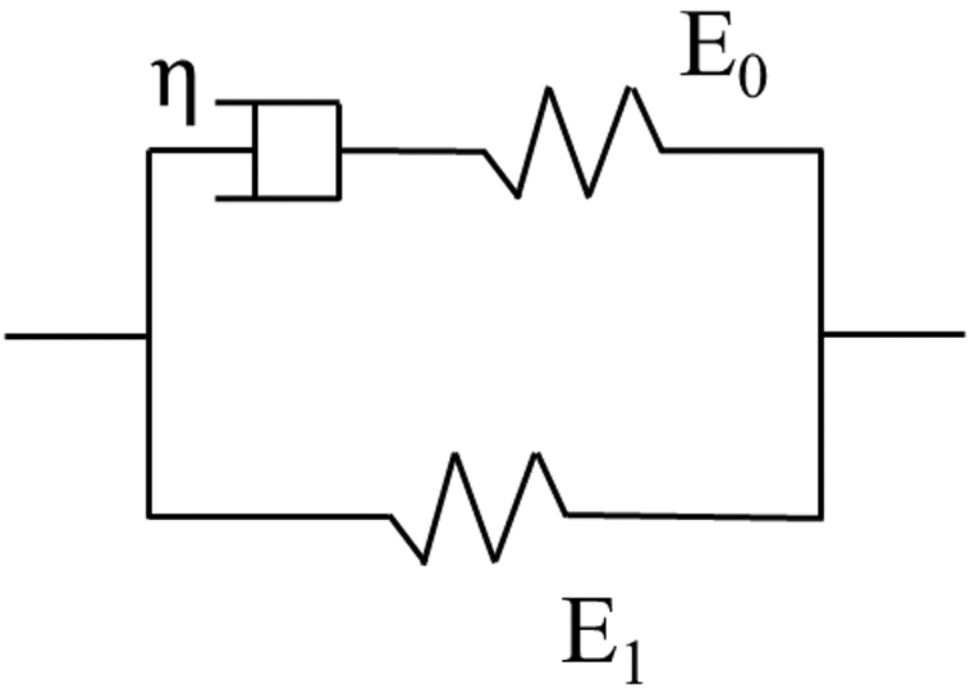

Figure A1.
An illustration of Three-element (Kevin-form) Standard Linear Solid (SLS) model. A spring (E_0) and a dashpot (η) are first connected in series (Maxwell body). Then the Maxwell body is connected with a spring (E_1) in parallel.

The strain **creep response curve** of the SLS model can be expressed as (29),

$$\varepsilon(\mathrm{t})=\varepsilon_0+\varepsilon_0\frac{\mathrm{E}_0}{\mathrm{E}_1}(1-\mathrm{e}^{-\frac{\mathrm{t}}{\tau_\sigma}}) \quad \text{(A3)}$$

where ε_0 is the instantaneous elastic strain that occurs immediately after compression, τ_σ is he relaxation time constant under a constant stress, and $\frac{E_0}{E_1}$ is γ_1 in Eqn. (A2) when N=1.

By adopting the QLV model, both the elastic and the viscous components affect the time-resolved stress and strain curves. In this study, both the Neo-Hookean model (24) and the Veronda-Westmann (V-W) model (30) were used. The Neo-Hookean model is close to a linearly elastic model, while the V-W model exhibits strain-stiffening behaviors observed in breast tissues (26). Particularly, the strain energy function of the V-W model can be written as follows,

$$W = C_1[e^{(C_2(I_1-3))} - 1] - \frac{C_1 C_2}{2}(I_2 - 3) + U(J) \quad \text{(A4)}$$

where C_1 and C_2 are, respectively, the first and second Veronda-Westmann coefficients, I_1 and I_2 are, respectively, the first and second invariant of the right Cauchy-Green tensor, and $U(J)$ is a function of volumetric strain function. In the FEBio(17), a nearly incompressible V-W model was implemented.

In this study, uniaxial stress-strain curves of glandular tissue, fat, skin, fibroadenoma and invasive ductal carcinoma were fit to the V-W model. Those stress-strain curves were derived based on previously published results (31-33). Material properties of the Cooper's ligament were derived from other ligament data in literature since stress-strain curve of Cooper's ligament is not available in the literature.

Table A1
Parameters associated with the elastic V-W model

Tissue Type	C_1 (kPa)	C_2
Fat	3	5
Fibro-glandular tissue	4	6.5
Cooper's ligament	25	7
Milk duct	3	2
Skin	300	5
Benign lesion	30	7
Malignant lesion	32	40
Lesion 1	30	7
Lesion 4	32	40

Parameters used for the relaxation function are shown in Table A2 below. Relaxation time values (were empirically chosen based on findings by Qiu et al. (11).

Table A2

Parameters related to the viscous component (*i.e.* relaxation function) of the QLV model (*i.e.* Eqns. (A1) and (A2)) used for Case 4 phantoms. Relaxation time constants (RTC) below are RTC values associated with the stress relaxation. Once those were converted to RTC values for strain creep, a factor of 1.95 should be used. This is well understood in the mechanics [*e.g.* (24)] and has been described in our previous publication (12) in the context of the SLS model.

Component	Viscoelastic coefficient (γ_1)	Relaxation time (τ_1) Unit: second
Fat	0.95	1
Fibro-glandular tissue	0.95	1
Cooper's ligament	0.95	1.5
Milk duct	0.95	1
Skin	0.95	1
Lesions 1 and 4	0.95	Varied

References

1. Ophir J, Cespedes I, Ponnekanti H, Yazdi Y, Li X. Elastography: a quantitative method for imaging the elasticity of biological tissues. Ultrasonic Imaging. 1991; 13(2):111–34. [PubMed: 1858217]
2. Hall TJ, Zhu YN, Spalding CS. In vivo real-time freehand palpation imaging. Ultrasound in Medicine and Biology. 2003; 29(3):427–35. [PubMed: 12706194]
3. Odonnell M, Skovoroda AR, Shapo BM, Emelianov SY. Internal Displacement and Strain Imaging Using Ultrasonic Speckle Tracking. Ieee T Ultrason Ferr. 1994; 41(3):314–25.
4. Burnside ES, Hall TJ, Sommer AM, Hesley GK, Sisney GA, Svensson WE, et al. Differentiating benign from malignant solid breast masses with US strain imaging. Radiology. 2007; 245(2):401–10. [PubMed: 17940302]
5. Jiang JF, Hall TJ. A Generalized Speckle Tracking Algorithm for Ultrasonic Strain Imaging Using Dynamic Programming. Ultrasound in Medicine and Biology. 2009; 35(11):1863–79. [PubMed: 19682789]
6. Zhu YN, Hall TJ. A modified block matching method for real-time freehand strain imaging. Ultrasonic Imaging. 2002; 24(3):161–76. [PubMed: 12503771]
7. Insana MF, Pellot-Barakat C, Sridhar M, Lindfors KK. Viscoelastic imaging of breast tumor microenvironment with ultrasound. J Mammary Gland Biol Neoplasia. 2004; 9(4):393–404. [PubMed: 15838608]
8. Sridhar M, Insana MF. Ultrasonic measurements of breast viscoelasticity. Med Phys. 2007; 34(12): 4757–67. [PubMed: 18196803]
9. Sridhar M, Liu J, Insana MF. Viscoelasticity imaging using ultrasound: parameters and error analysis. Phys Med Biol. 2007; 52(9):2425–43. [PubMed: 17440244]
10. Sridhar M, Liu J, Insana MF. Elasticity imaging of polymeric media. J Biomech Eng. 2007; 129(2): 259–72. [PubMed: 17408331]
11. Qiu Y, Sridhar M, Tsou JK, Lindfors KK, Insana MF. Ultrasonic viscoelasticity imaging of nonpalpable breast tumors: preliminary results. Acad Radiol. 2008; 15(12):1526–33. [PubMed: 19000869]
12. Wang Y, Helminen E, Jiang J. Building a virtual simulation platform for quasistatic breast ultrasound elastography using open source software: A preliminary investigation. Med Phys. 2015; 42(9):5453–66. [PubMed: 26328994]
13. Kallel F, Bertrand M, Ophir J. Fundamental limitations on the contrast-transfer efficiency in elastography: an analytic study. Ultrasound Med Biol. 1996; 22(4):463–70. [PubMed: 8795173]

14. Varghese T, Ophir J. An analysis of elastographic contrast-to-noise ratio. Ultrasound Med Biol. 1998; 24(6):915–24. [PubMed: 9740393]
15. Bharat S, Varghese T. Contrast-transfer improvement for electrode displacement elastography. Phys Med Biol. 2006; 51(24):6403–18. [PubMed: 17148825]
16. Bhatti SN, Sridhar-Keralapura M. A novel breast software phantom for biomechanical modeling of elastography. Med Phys. 2012; 39(4):1748–68. [PubMed: 22482599]
17. Maas SA, Ellis BJ, Ateshian GA, Weiss JA. FEBio: Finite Elements for Biomechanics. J Biomech Eng-T Asme. 2012; 134(1)
18. Pavan TZ, Madsen EL, Frank GR, Jiang J, Carneiro AA, Hall TJ. A nonlinear elasticity phantom containing spherical inclusions. Phys Med Biol. 2012; 57(15):4787–804. [PubMed: 22772074]
19. Schroeder, W., M, K., Lorensen, B. The visualization toolkit. Prentice Hall PTR; Upper Saddle River, NJ: 1998.
20. Si H, Gartner K. 3D boundary recovery by constrained Delaunay tetrahedralization. Int J Numer Meth Eng. 2011; 85(11):1341–64.
21. National_Library_of_Medicine. The Visible Human Project Getting the Data. 2000
22. Fung, YC. Biomechanics : mechanical properties of living tissues. 2nd. New York: Springer-Verlag; 1993. p. xviii, 568
23. Ophir J, Alam SK, Garra B, Kallel F, Konofagou E, Krouskop T, et al. Elastography: ultrasonic estimation and imaging of the elastic properties of tissues. Proceedings of the Institution of Mechanical Engineers Part H-Journal of Engineering in Medicine. 1999; 213(H3):203–33.
24. Fung, YC. Biomechanics : mechanical properties of living tissues. 2nd. New York: Springer-Verlag; 1993. p. xviii, 568
25. Ponnekanti H, Ophir J, Huang Y, Cespedes I. Fundamental mechanical limitations on the visualization of elasticity contrast in elastography. Ultrasound Med Biol. 1995; 21(4):533–43. [PubMed: 7571146]
26. Kallel F, Ophir J, Magee K, Krouskop T. Elastographic imaging of low-contrast elastic modulus distributions in tissue. Ultrasound Med Biol. 1998; 24(3):409–25. [PubMed: 9587996]
27. Itoh A, Ueno E, Tohno E, Kamma H, Takahashi H, Shiina T, et al. Breast disease: clinical application of US elastography for diagnosis. Radiology. 2006; 239(2):341–50. [PubMed: 16484352]
28. Maas SA, Ellis BJ, Ateshian GA, Weiss JA. FEBio: Finite Elements for Biomechanics. Journal of Biomechanical Engineering. 2012; 134(1):011005–10. [PubMed: 22482660]
29. Ethier, CR., Simmons, CA. Introductory biomechanics from cells to organisms. Cambridge; New York: Cambridge University Press; 2007. Available from: http://app.knovel.com/web/toc.v/cid:kpIBFCO008
30. Veronda DR, Westmann RA. Mechanical characterization of skin—Finite deformations. Journal of biomechanics. 1970; 3(1):111–24. [PubMed: 5521524]
31. Krouskop TA, Wheeler TM, Kallel F, Hall T. The elastic moduli of breast and prostate tissues under compression. Ultrasonic Imaging. 1998; 20:260–74. [PubMed: 10197347]
32. Wellman PS, Dalton EP, Krag D, Kern KA, Howe RD. Tactile imaging of breast masses: first clinical report. Arch Surg. 2001; 136(2):204–8. [PubMed: 11177142]
33. Bigelow TA. Improved algorithm for estimation of attenuation along propagation path using backscattered echoes from multiple sources. Ultrasonics. 2010; 50(4-5):496–501. [PubMed: 19913861]

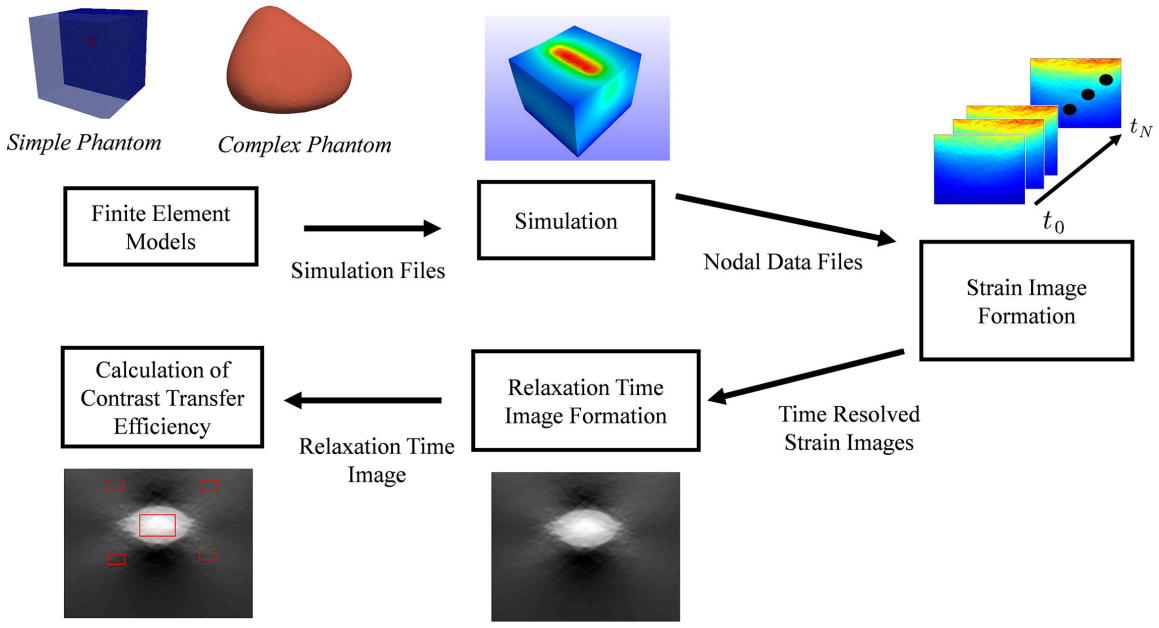

Figure 1.

Software workflow for generating simulated creep/relaxation time images. In the first step, model geometries and finite element meshes were created using open-source software packages (VTK and Tetgen). In the second step, the intended FEA simulation was performed using an open-source FE package (*i.e.* FEBio) to mimic VEI data acquisition (*i.e.* strain creep under a constant compression). In the third step, FE-simulated displacement data were processed to obtain a sequence of time-resolved strain images. In the fourth step, relaxation time constants were estimated from those aforementioned time-resolved strain data. In the last step, regions of interest (ROIs; *i.e.* red boxes in the subplot located at the lower left corner) were selected similarly as was done in (12, 18). Imaging contrast values were then calculated from the selected ROI's and CTE evaluated for each and every VEI image.

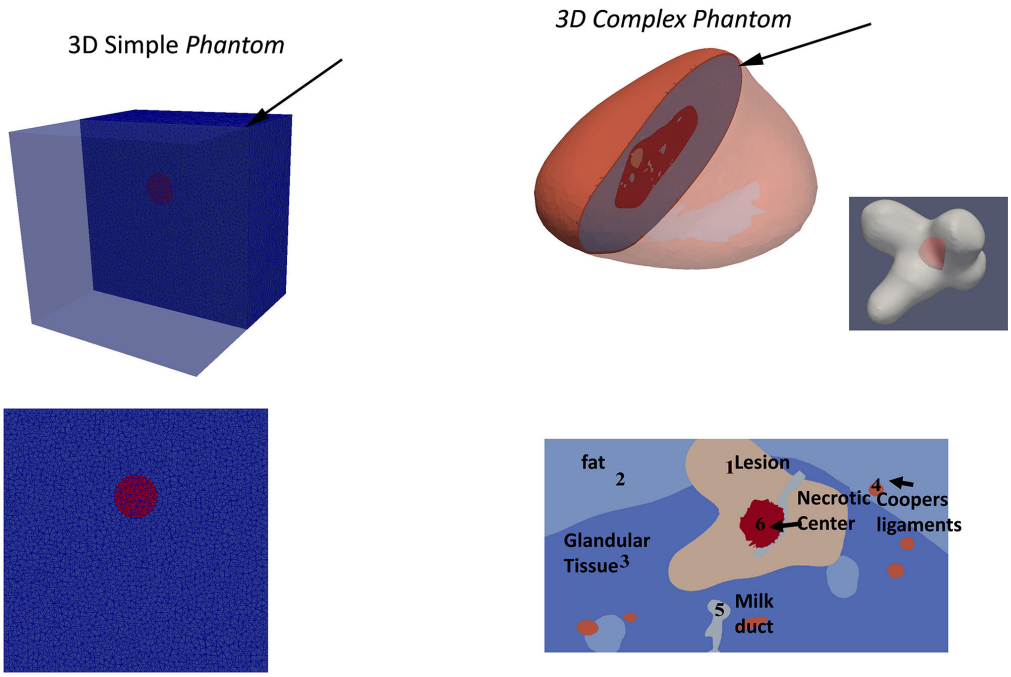

Figure 2.

Two illustrative examples of 3D numerical breast phantoms by which FE simulations were performed. The left and right columns show a simple numerical phantom and a complex heterogeneous phantom, respectively. Arrows on both top plots point to the image planes within the respective 3D volumes, while those two image planes are displayed in the bottom plots. The complex breast phantom shown above is the same as the Lesion 4 phantom used in a previous publication (12).

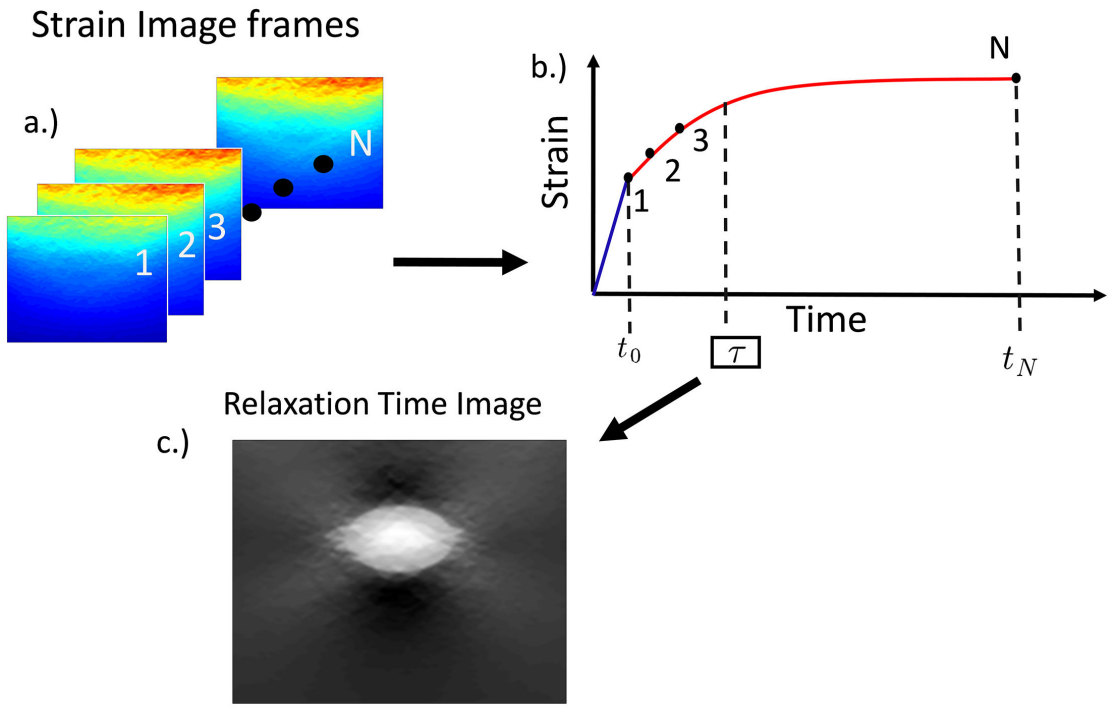

Figure 3.

An illustration of the image formation process related to the assessment of the relaxation time constant: (a) A series of time-resolved strain images is formed, (b) one relaxation time curve at a spatial location/pixel is fitted to *N* frames starting at t_0, which is time at the end of the initial ramp force, and ending at t_N. In (c), the resultant relaxation time constant (RTC) image is shown.

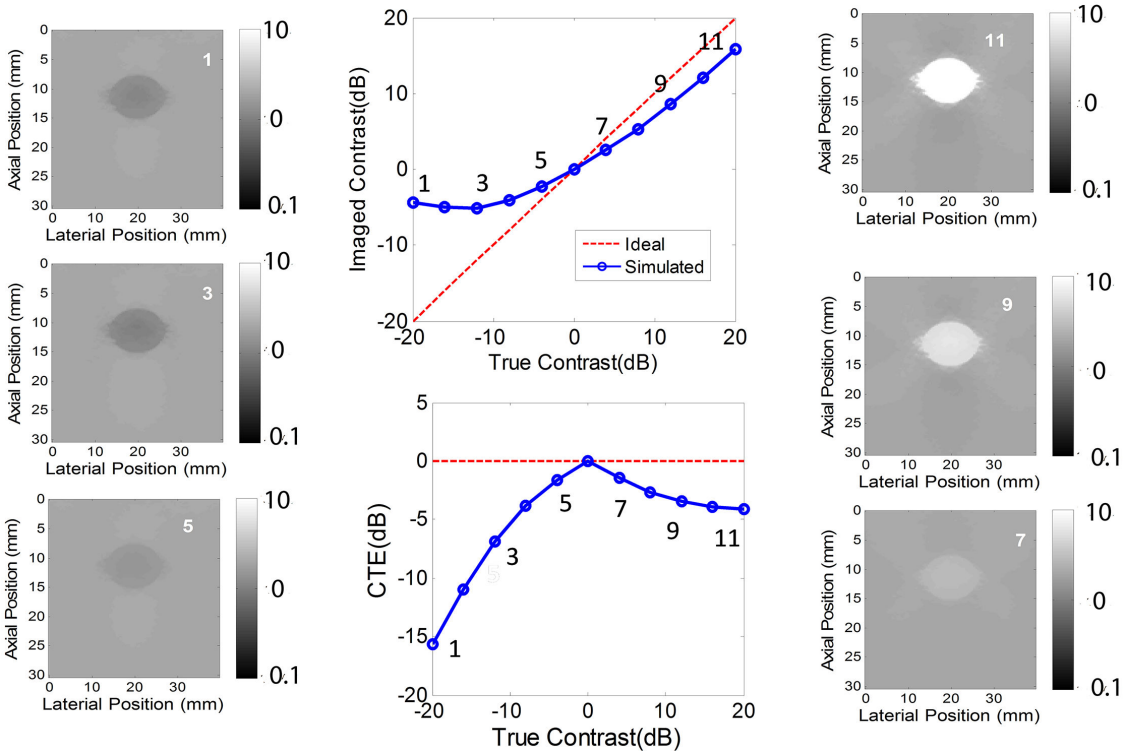

Figure 4.

Resultant plots and images showing contrast transfer characteristics in Case 1 phantoms. In the top middle plot, estimated image contrasts are plotted against the true contrast (in dB). In the lower middle plot, CTE is plotted against the true contrast. In both middle plots, simulation results are plotted in blue while the ideal contrast transfer is represented by a dashed red line. In the left and right columns, FE-simulated RTC images were shown corresponding to the numbered points on those two blue curves in the two middle plots. The units in all RTC images were time (seconds).

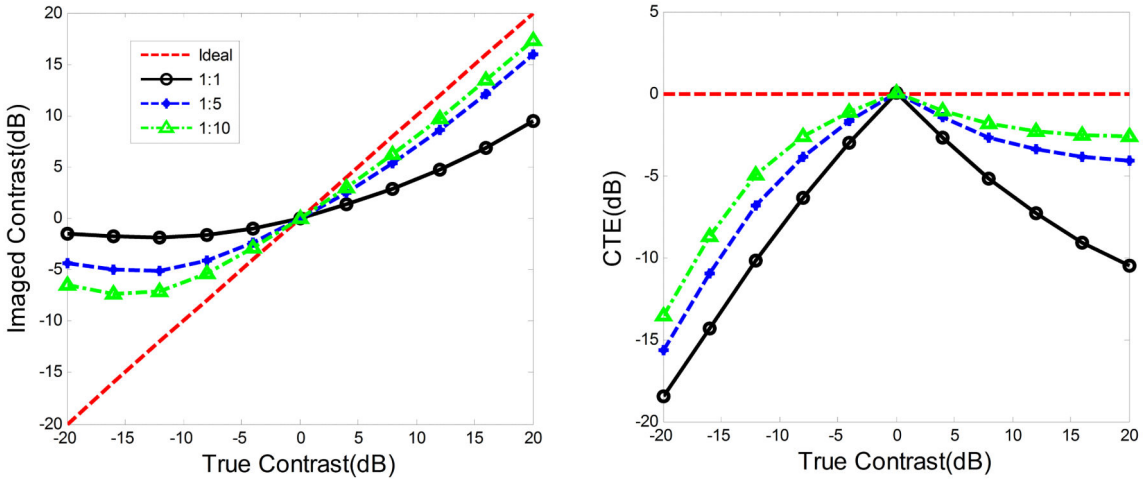

Figure 5.

Two plots showing contrast transfer characteristics in Case 1 phantoms with the increase of elastic ratio between the target and the background (from 1:1 to 10:1). In the left plot, estimated image contrasts are plotted against the true contrast (in dB). In the right plot, CTE is plotted against the true contrast. In both plots, simulation results are plotted in blue while the ideal contrast transfer is represented by a dashed red line.

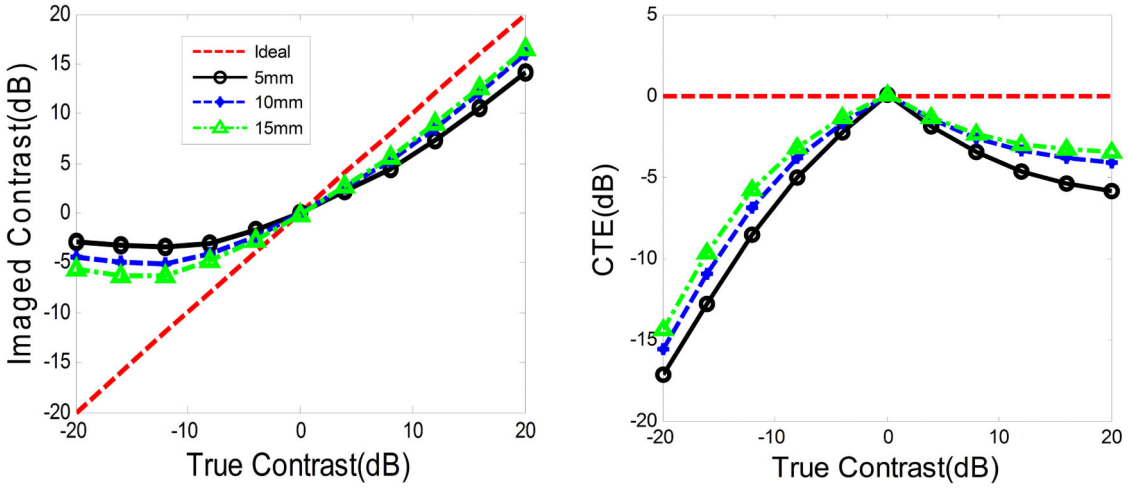

Figure 6.

Two plots showing contrast transfer characteristics in Case 2 phantoms with three different sized targets (from 5 mm diameter to 15 mm diameter). In the left plot, estimated image contrasts are plotted against the true contrast (in dB). In the right plot, CTE is plotted against the true contrast. In both plots, simulation results are plotted in blue while the ideal contrast transfer is represented by a dashed red line.

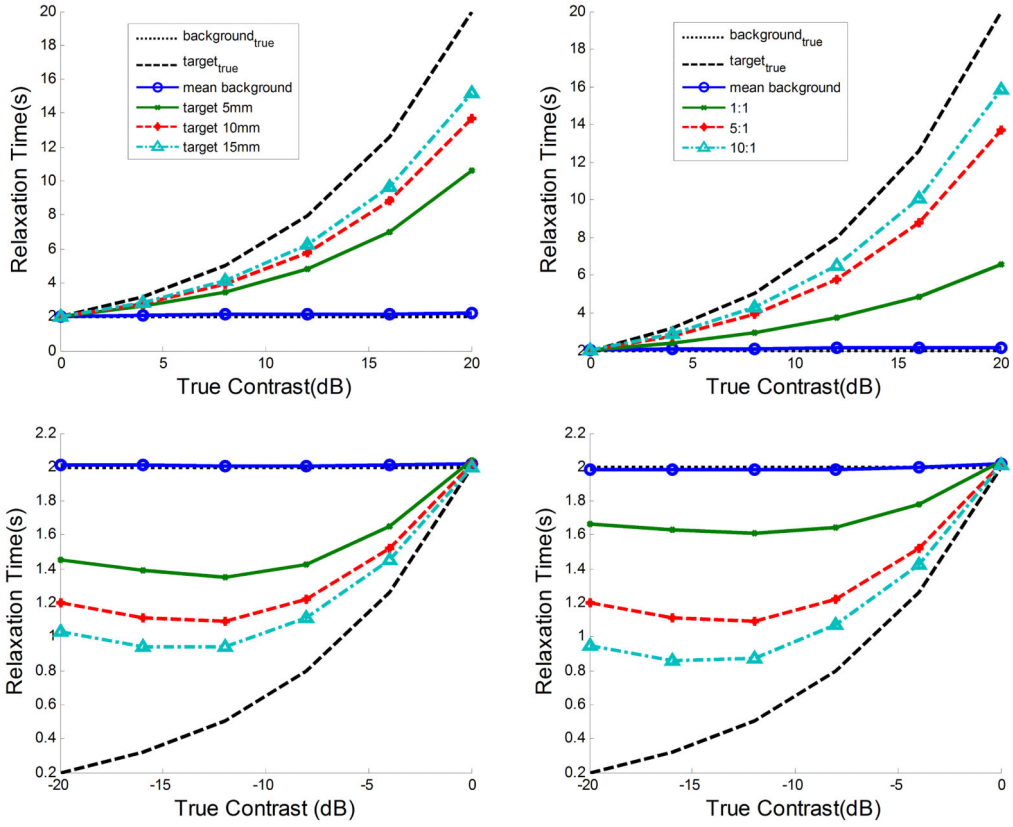

Figure 7.

Relaxation time as a function of true contrast in the Case 2 phantom. Results are cut apart into separate plots for -20dB to 0dB (top row) and 0dB to 20dB (bottom row) for easier viewing. Note that since background relaxation time constants deviated unappreciable from each other, only a mean values for the background relaxation time is plotted.

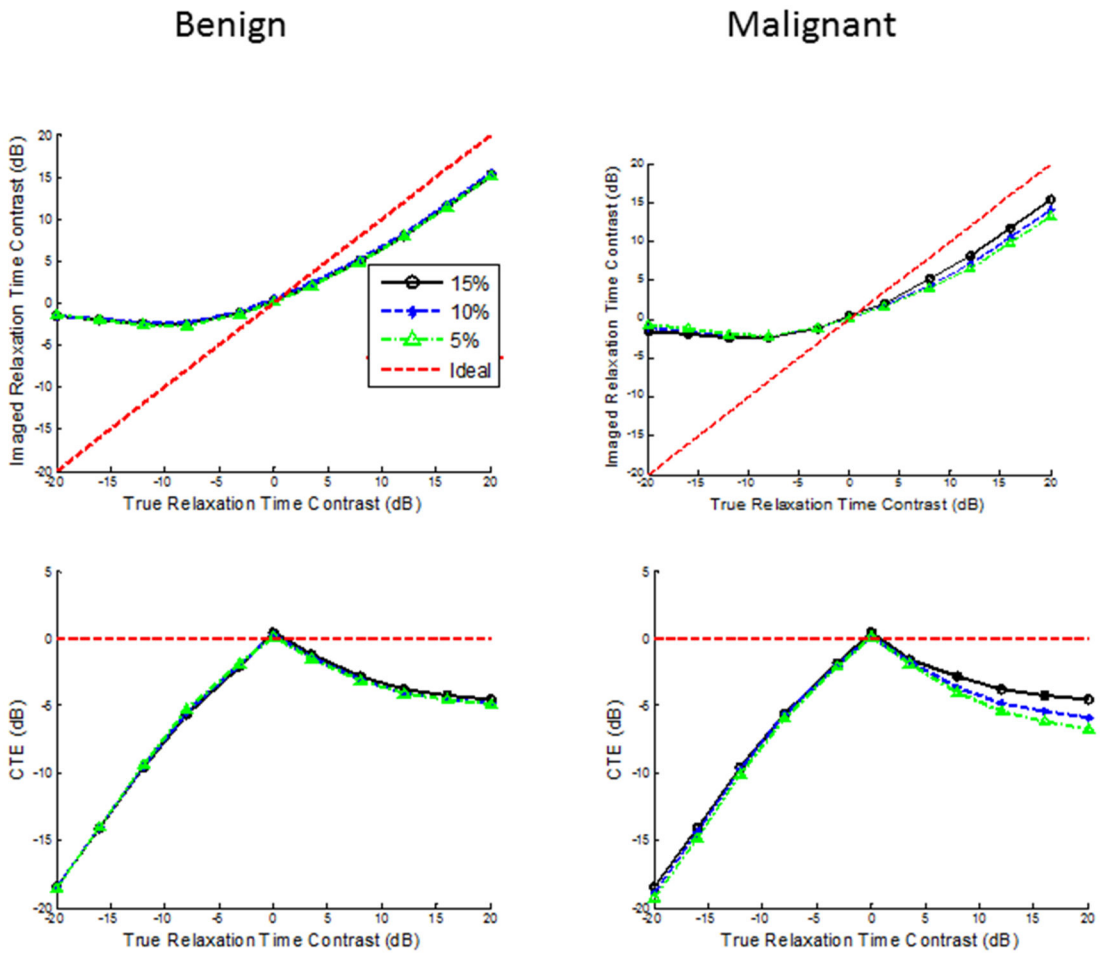

Figure 8.

Contrast transfer characteristics for two Case 3 Phantoms which represent different non-linear elastic stress-strain curves (using the VW hyperelastic model). Simulations were ran to a deformation level of 5% (black curves) 10% (blue curves) and 15% (green curves). The leftmost plots are of simulations using material parameters characteristics of a (simulated) benign lesion and the rightmost plots are that of a (simulated) malignant lesion.

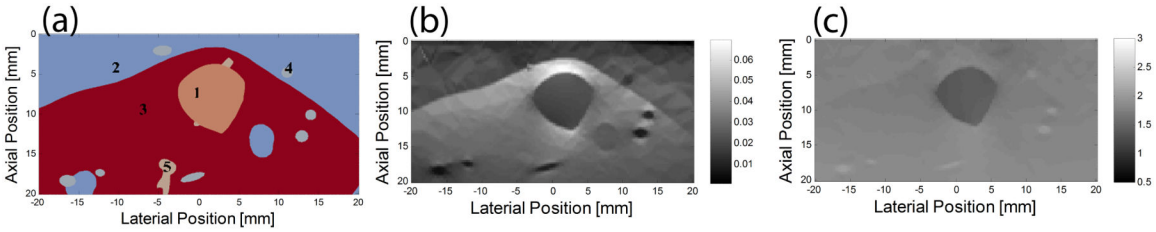

Figure 9.

Results from the Lesion 1 phantom: (a) tissue composition of the image plane, (b) FE-simulated axial strain image and (c) RTC image. In (a), 1-5 denote lesion, breast fat, fibro-glandular tissue, cooper's ligaments and milk ducts, respectively. In (c), the unit of the color bar is time (seconds).

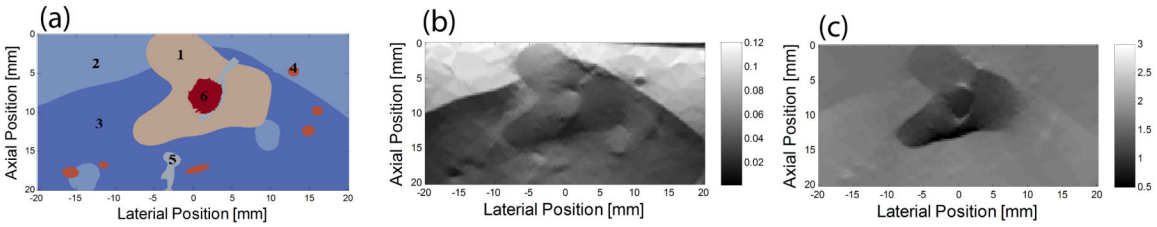

Figure 10.

Results from the Lesion 4 phantom: (a) tissue composition of the image plane, (b) FE-simulated axial strain image and (c) RTC image. In (a), 1-6 denote lesion, breast fat, fibro-glandular tissue, cooper's ligaments, milk ducts and necrotic core, respectively. In (c), the unit of the color bar is time (seconds).

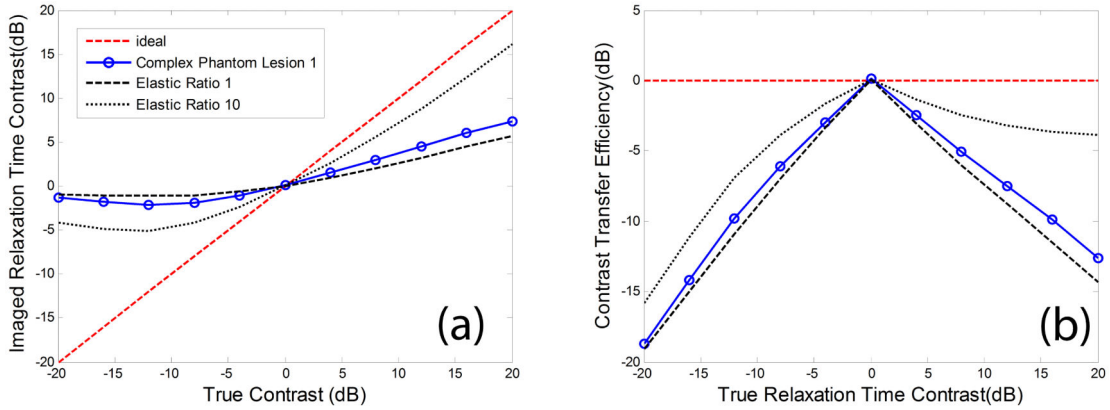

Figure 11.

Results showing contrast transfer characteristics of Lesion 1 phantom: (a) estimated contrasts plotted against the true contrast (in dB) and (b) CTE plotted against the true contrast. Simulation results are plotted in blue while the ideal contrast transfer is represented by a dashed red line. In (a) and (b), contrast transfer characteristics curves (*i.e.* black dashed and dotted lines) from Case 1 phantom is also included.

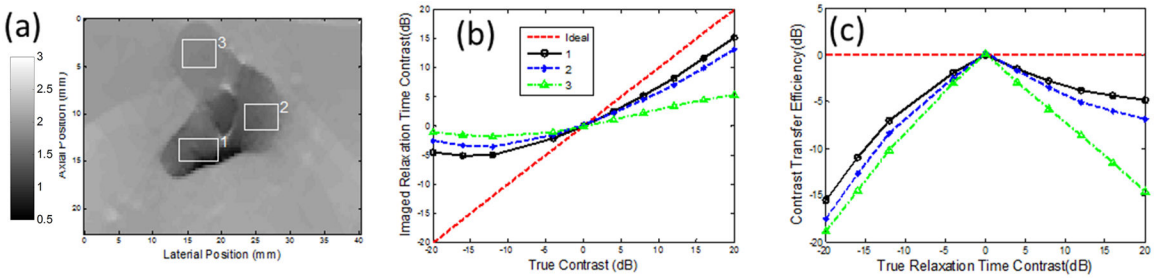

Figure 12.

Regional characteristics of contrast transfer in Lesion 4 Phantom: (a) a RTC image of the complex Lesion 4 phantom, (b) a plot of resulting imaged contrast versus true contrast and (c) CTE curves for three selected regions shown in (a).

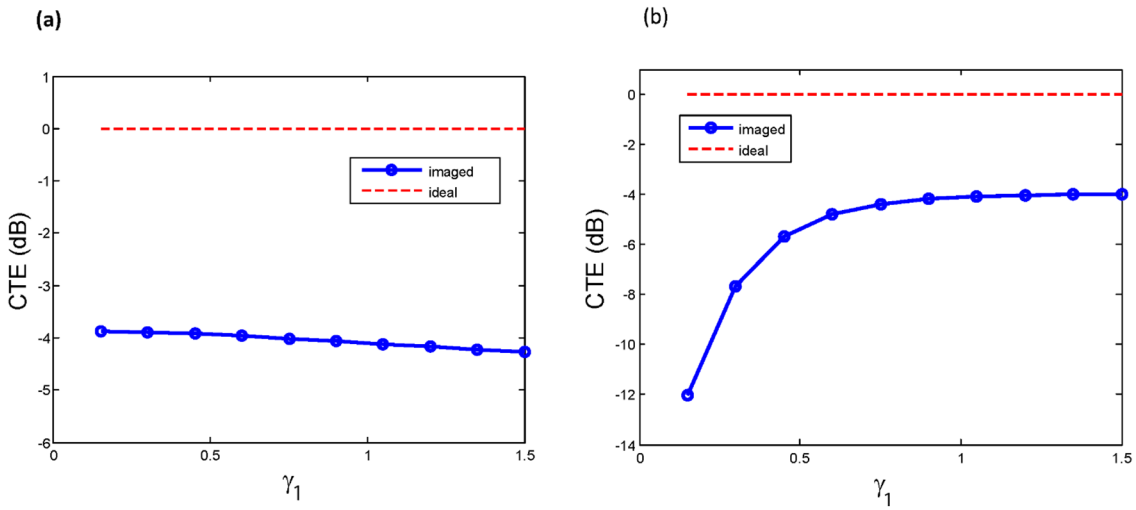

Figure 13.

Plots showing CTE with varied γ parameters in Case 1 Phantom: (a) γ_1 varied identically between imaging target and background and (b) γ_1 varied within imaging target only while background was held at a constant 1.

Table 1

Descriptions of FE-simulation Models including boundaries conditions and essential material properties. The values for the relaxation time constant (RTC) reported below were converted from RTC values under stress relaxation. More details of this conversion can be found in Appendix A of a prior publication (12). RTC values of background materials were derived from (11).

Model Description	Boundary Conditions	Viscous Component in the QLV model	Elastic Component in the QLV model
Case 1 (Simple Phantom)	A compression was ramped over 1 second to 5% of deformation and was maintained to simulate strain creep	The relaxation time constant (RTC) of the background was set to 2seconds and the RTC values of the target were varied such that C_t fell between -20dB to 20 dB; =0.95 (Eqn. A2 in Appendix) for most cases except results presented in Section 3.4.	Neo-Hookean Model with Poisson's ratio of 0.49 and an initial elastic modulus of 30 kPa (23) for the background material. Initial elastic modulus ratios between the inclusion and the background varied (1:1, 5:1, 10:1)
Case 2 (Simple Phantom)	Same as Case 1	Same as Case 1	Neo-Hookean Model with Poisson's ratio of 0.49 and an initial elastic modulus of 30 kPa (23) for the background material. Initial elastic modulus ratio between the inclusion and the background was fixed (5:1). The inclusion diameter was varied (5 mm, 10 mm and 15 mm).
Case 3 (Simple Phantom)	One pre-compression load (5%, 10% or 15%) was first applied within 1 s, followed by a 2% compression within 1s. The force was maintained to simulate strain creep	Same as Case 1	Veronda-Westmann (V-W) model; material properties for background was that of healthy glandular tissue and properties of the inclusion were that of simulated benign and malignant tumors. (see Table A1 of Appendix)
Case 4 (Lesion 1 and Lesion 4 Phantoms)	A compression was ramped over 1 second to 5% of deformation and was maintained to simulate strain creep	Fixed the background glandular tissue with a RTC value of 2 seconds; varied the RTC values of lesions so that C_t was between -20dB to 20 dB; RTC values for the rest tissue types can be found in Table A2	V-W model (see Tables A1 and A2)